Chpater-6

Direct Visualization of Carrier Motion in DPP-TTT/C_3N_5 Blended Organic Thin Film Transistor by Optical Second-Harmonic Generation.

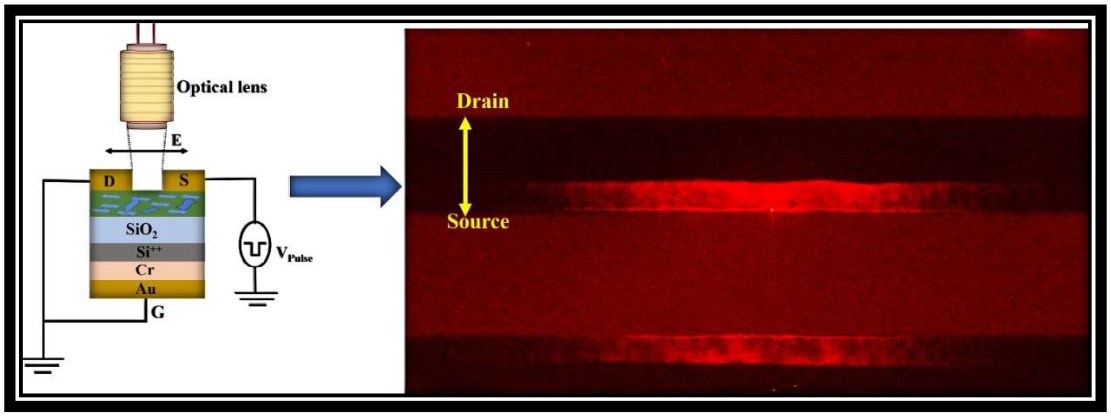

This chapter focuses on the fabrication of DPP-TTT/C3N5 polymer nanocomposite thin films at the air-liquid interface using the UFTM. It further explores charge transport studies through Time-Resolved Second Harmonic Generation (TRM-SHG), providing insights into how C_3N_5 nanosheets influence and enhance charge transport in the nanocomposite films.

6.1. Introduction

Materials falling under the classification of organic-inorganic and organic hybrids, which include diverse nanofiller types, are currently witnessing a significant boost in performance, particularly in the realm of OFETs and optoelectronic devices [52, 172-174]. The enhanced performance is a result of their unique optical and electrical properties [175]. Additionally, these materials offer the advantage of easy processing in solution, further contributing to their growing prominence in these applications [54]. Recent advancements in charge carrier movement between organic and inorganic materials have significantly enhanced device performance[52, 106, 176]. Inorganic materials, with their ultra-flat surfaces and high carrier mobility, serve as excellent substrates for organic materials, ensuring sharp interfaces and superior charge transportation[53, 175]. This synergy has led to the development of high-performance electronic and optoelectronic devices. Organic materials, known for their tunable optical absorption, have improved 2D TMDC photodetectors like MoS_2 and WSe_2 by extending their spectral detectivity range and enhancing responsivity and charge dissociation[177]. Additionally, organic materials help tune the electronic properties of inorganic materials, acting as n-type and p-type dopants and facilitating defect healing in sulphury-containing transition metal dichalcogenides (TMDCs). This results in better carrier mobility for FETs and makes organic-inorganic heterostructures ideal for efficient solar cells due to ultra-fast charge carrier dissociation and slow recombination[52]. These advancements demonstrate the potential of hybrid materials in creating superior electronic and optoelectronic devices. Despite the rapid advancements in applications involving organic–inorganic and organic hybrids with nanofiller types, certain ambiguous behavior still poses challenges that require comprehensive understanding[40, 52, 54]. These include notable current–voltage hysteresis[178], the prevalence of ion migration[179], trapping and detrapping

effects[180]. Traditional methodologies have offered considerable insights into the electrical properties of OTFTs, predominantly through indirect measurements that infer carrier dynamics from macroscopic device behaviors [181-183]. However, the intrinsic complexity and heterogeneity of organic semiconductors, compounded by the critical influence of microstructural features and interfaces on charge transport, call for more direct and refined investigative techniques.

To address these issues, a focused examination of fundamental carrier behaviours such as injection, transport, and the nature of photogenerated species is crucial. Current research efforts are intensely focused on uncovering the basic optical and electrical characteristics of organic-inorganic hybrid materials. Specifically, there is a concerted effort to directly observe carrier injection from the electrode and understand its transport mechanisms. This approach is deemed essential for gaining a deeper insight into the intricate carrier behavior exhibited by these organic hybrid materials. The study of carrier motion within various materials is a crucial area of interest that spans the disciplines of physics, materials science, electronics, and electrical engineering[184]. The investigation into this phenomenon leverages a variety of electrical techniques, significantly advancing our comprehension of the underlying principles that dictate material behavior. This, in turn, influences a broad array of scientific and technological fields. At the heart of these investigative techniques is the principle of indirectly studying carrier motion and related electrical phenomena[32]. Tools such as electrometers are used for this purpose. Among the various methods utilized, the Time-of-Flight (TOF) technique stands out for its effectiveness in measuring the drift mobility of a wide range of materials, including both inorganic amorphous solids and organic compounds[70, 185]. In the TOF method, the observation of Maxwell's displacement current in an external circuit act as an indirect probe into the carrier motion over long distances within the material. This process involves the creation of a thin carrier

sheet via light-pulse irradiation near one electrode, which then drifts towards the opposite electrode under the influence of an applied electric field. The journey of this carrier sheet through the material alters the induced charge at the counter electrode, with these changes being monitored through transient current measurements. This allows for the indirect observation of the carrier sheet's motion, from which the drift mobility is calculated by dividing the material's thickness by the product of transit time and the applied electric field. Additionally, the transient current trace analysis offers insights into carrier traps within the material, making TOF measurements particularly valuable for studying devices like OFETs [186]. However, the indirect nature of this technique necessitates a sophisticated mathematical approach for current pulse analysis, presenting challenges in accurately replicating observed pulses, especially in scenarios involving multiple carrier traps or the differentiation between carrier-injection and carrier-transport processes. This complexity is not unique to the TOF method but is shared by other electrical techniques that indirectly assess carrier motion, such as pressure-wave propagation and pulsed electro-acoustic methods. These methods face a fundamental challenge due to their dependence on indirect measurements, highlighting the necessity for a technique that can directly examine carrier motion. To meet this requirement, we employed an optical strategy to directly observe carrier motion in organic thin films. This was achieved through the use of time-resolved microscopic optical second harmonic generation (TRM-SHG) [187, 188]. This technique uses a highly sensitive cooled CCD camera to capture time-resolved SHG images of organic thin films. TRM-SHG relies on the non-destructive interrogation of locally induced electric fields within materials via a two-photon process[31]. This methodology's applications span various devices, including OFETs and organic electroluminescence (EL) devices. It provides crucial information for simulating carrier movement in both organic insulators and semiconductors.

In this work, I successfully synthesized C_3N_5 and used a mechanical exfoliation technique to generate C_3N_5 nanosheets from the bulk materials. These nanosheets were then utilized as a filler in the fabrication of an OFETs using the DPP-TTT polymer. The fabrication process involved the application of the Unidirectional Floating Film Transfer Method (UFTM), known for its efficiency in producing extensive, uniform, and well-aligned thin films of conducting polymers (CPs). The UFTM process begins with the fabrication of oriented and durable thin films on a liquid substrate positioned orthogonally. Subsequently, these films are seamlessly transferred onto the desired substrate. Notably, a study by Syafutra et al [145]. highlighted that UFTM films exhibit a consistent orientation throughout their entire thickness, making them highly suitable for diverse device geometries. In our work, we harnessed the advantages of UFTM films by using them as the active layer in the fabrication of the OFETs. The charge carrier dynamics of these OFETs were thoroughly investigated using TRM-SHG, providing valuable insights into the performance and behavior of the devices. This study enhances our knowledge of the dynamics of charge carriers and the influence of C_3N_5 nanosheets on the charge transport behavior in devices based on DPP-TTT conjugated polymers. This advanced methodology allows us to precisely elucidate the charge transport behavior within the polymer and accurately determine the inherent charge transport capabilities of the charge carriers, underscoring the intrinsic properties of these materials.

6.2. Materials and Methods:

6.2.1. Materials:

Poly[2,5-(2-octyldodecyl)-3,6-diketopyrrolopyrrole-alt-5,5-(2,5-di(thien-2-yl)thieno[3,2-b]thiophene)], commonly known as DPP-TTT, was purchased from Ossilla Co. With a chemical composition of $(C_{60}H_{88}N_2O_2S_4)n$, it possesses an average molecular weight of

183 KDa, and its chemical structure is ***shown in Figure 2.1(a).*** The CAS number assigned to this polymer is 1260685-66-2. DPP-TTT is notably recognized for its ease of processing and resilience to environmental conditions, making it a valuable material for various applications. Ethylene glycol, glycerol, and chloroform were sourced from Sigma Aldrich, while a SiO_2 wafer with a thickness of 300nm was obtained from Global Nanotech Ltd.

6.2.2. Preparation of Exfoliated C_3N_5 Nanosheets from Bulk C_3N_5:

The synthesis of C_3N_5 is detailed in ***chapter 2 section 2.3.1.*** To exfoliate C_3N_5 into few-layered nanosheets, a 5 mg sample of bulk C_3N_5 was dispersed in 2 ml of water and then subjected to vigorous probe sonication for a period of 3 hours, ensuring comprehensive dispersion and transformation of the bulk material into nanosheets [63]. After the sonication step, the resultant material was carefully centrifuged to separate the larger C_3N_5 particles from the exfoliated few-layered C_3N_5. The separated bulk components were then dried and weighed to determine the yield of nanosheets. To ensure that only the portion rich in nanosheets is used, the homogeneous supernatant solution, free from larger particles and impurities, was extracted and utilized as the initial material for subsequent experimental procedures.

6.2.3. Thin Film Fabrication:

Next, to fabricate the DPP-TTT/C_3N_5 nanohybrid thin film, the process was initiated by preparing a polymer-nanohybrid solution with a 10 mg/ml concentration in chloroform. First, a homogeneous chloroform dispersion of C_3N_5 and polymeric chloroform solution of DPP-TTT (10 mg/ml) was prepared separately. After that, 4 separate well-integrated hybrid blends of DPP-TTT and C_3N_5(x) (x: 0%, 1%, 3%, 5%) were prepared through prolonged stirring inside well-packed Teflon-capped glass vials. As C_3N_5 nanosheets were used as a filler material in the D-A type polymer matrix, the percentage of C_3N_5 was kept below 10%. Since thin film characterizations, exfoliated C_3N_5 nanosheets are termed as C_3N_5.

Thin films of these hybrid solutions were fabricated using a cost-effective method, *UFTM* [127]. This method comprises steps of preparation of a warm (40 °C) hydrophilic liquid mixture of ethylene glycol and glycerol (1:1 in V/V); spreading around 15-20 µl of the hydrophobic DPP-TTT/C_3N_5 nanohybrid solution, 'CP ink', onto the surface of the liquid substrate; lifting the developed thin solid film floating over the air-liquid interface over substrates of choice; thorough washing of the films with methanol and isopropyl alcohol to remove any liquid residue and then annealing at 110 °C under N_2 atmosphere to fabricate the final thin film. In this method, the spontaneous spreading of the polymeric solution was governed by the Marangoni effect, and to guide the spreading in one direction, a Teflon slider was used, as illustrated in ***Figure 2.5(a)*** During the spreading of the solution, chloroform evaporates rapidly, and a dried thin solid film was found floating like a semi-transparent ribbon ***Figure 2.5(b).*** Notably, UFTM films of conducting polymers (CPs) that contain hydrophobic alkyl side chains, exhibit a preference for adopting an edge-on type molecular packing [66]. This identical methodology was employed for fabricating thin films used in structural and optical characterization, as well as in the fabrication of (FETs).

6.2.4 Device Fabrication:

Organic Field-Effect Transistors (OFETs) were fabricated on highly p-doped Si/SiO_2 substrates with a SiO_2 thickness of 300 nm. The substrates underwent a thorough cleaning process, starting with using Hellmanex solution, followed by two rounds of hot double-distilled water rinsing. The process was extended by ultrasonically cleaning the material in acetone and isopropyl alcohol (IPA) for 10 minutes each, followed by baking at 120 °C for 30 minutes. Next, the substrates were immersed in hot (110 °C) octadecyl trichlorosilane (ODTS) solution (10 mM) in toluene for 2 hours, followed by thorough rinsing with toluene and annealing at 100 °C for 30 minutes. Nanohybrid thin films prepared through *UFTM*,

were then transferred onto the substrates as described previously. Along with a strong moisture repelling behaviour, ODTS treatment facilitates the adhesion between polymeric thin film and the substrates. In the final step, gold source and drain electrodes, 60 nm in thickness and with channel dimensions of (2.8 mm in width and 30μm in length), were deposited through thermal evaporation using a nickel shadow mask. Fabricated OFETs were measured at room temperature under 50% relative humidity conditions in a light-attenuated environment, utilizing a Keithley-2612 source measure unit (SMU).

6.3. Results and Discussion

6.3.1 Characterization of C_3N_5:

6.3.1.1 XRD Analysis:

To validate the crystal structure and synthesis of C_3N_5, first, a powder XRD pattern has been recorded using the Rigaku Smart Lab system, operating at 40 kV with a diffraction angle range between 5-70 degrees.

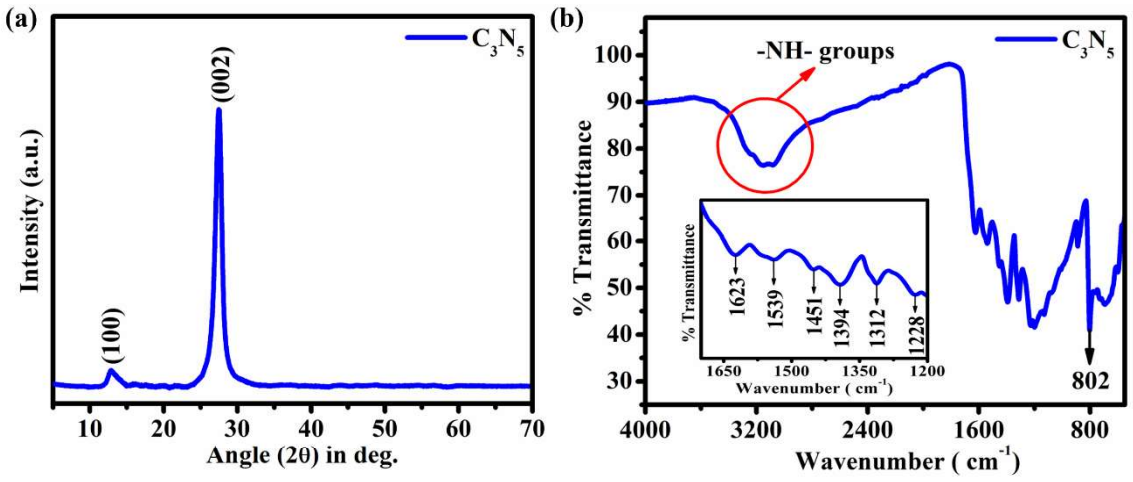

Figure 6. 1 (a) *XRD pattern of the bulk C_3N_5,* ***(b)*** *FTIR spectra of C_3N_5.*

The XRD pattern for C_3N_5, as shown in ***Figure 6.1(a)***, displayed a prominent characteristic peak, denoted as (002), occurring at 2θ = 27.7 degrees. This peak is indicative of the presence of stacked aromatic systems along the *c*-axis. Additionally, a relatively weaker

diffraction peak, designated as (100), was observed at 13.4 degrees. This peak corresponds to the repeat unit of triazole. Thus, comparing with reported literatures[63, 189], XRD pattern indicates the successful formation of bulk C_3N_5.

6.3.1.2. FTIR Analysis:

Next, the functional groups present in C_3N_5 were examined through the FTIR spectrum. Within the spectrum of ***Figure 6.1(b)***, a broad peak can be seen spanning the range of 3000-3600 cm^{-1}, which is associated with the stretching vibration of surface-free amino groups and the hydroxyl group of water[62, 63]. Furthermore, distinctive peaks were identified at specific wavenumbers: 1228 cm^{-1}, 1312 cm^{-1}, 1394 cm^{-1}, 1451 cm^{-1}, 1539 cm^{-1}, and 1623 cm^{-1}. These peaks correspond to the typical stretching vibrations of C=N and C-N heterocycles, which are indicative of specific functional groups within the material[190, 191]. Additionally, a peak observed at 807 cm^{-1} corresponds to the characteristic stretching vibration of the s-triazine ring unit.

6.3.1.3. Optical Analysis:

The optical characteristics of C_3N_5 powders were then investigated through the UV-Vis-Spectroscopy, and the spectral data has been presented in ***Figure 6.2(a).***

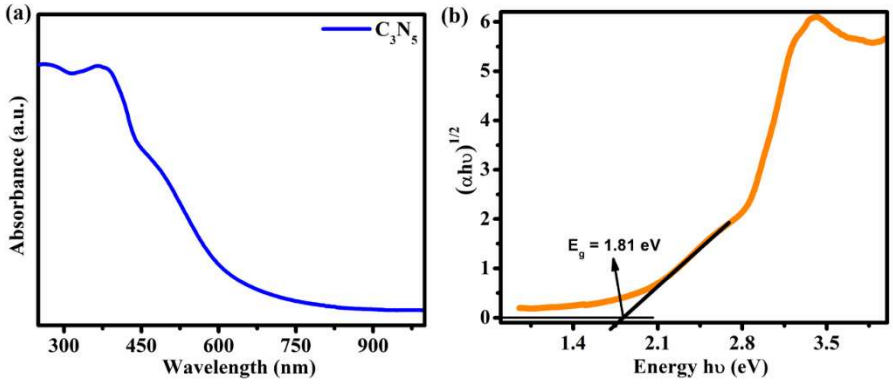

Figure 6. 2 (a) *UV-visible absorption spectra of C_3N_5* ***(b)*** *transformed Kubelka-Munk function versus photon energy for C_3N_5*

The absorption edge for C_3N_5 was noted to be around 700 nm, indicating significant absorption within the visible spectrum. The band gap of the synthesized material was estimated by analyzing the points of intersection of tangents, as depicted in ***Figure 6.2(b)***, using the Tauc equation [62, 63]. The band gap for C_3N_5 was determined to be 1.81 eV, which aligns with values reported in earlier scientific literature[63].

6.3.1.4. Xray Photo Spectroscopy (XPS):

Furthermore, X-ray photoelectron spectroscopy (XPS) was utilized to analyze the chemical composition and valence states of the elements on the surface of the synthesized material. In ***Figure 6.3(c)***, the survey scan shows only the presence of carbon, nitrogen, and some environmental adsorbed oxygen.

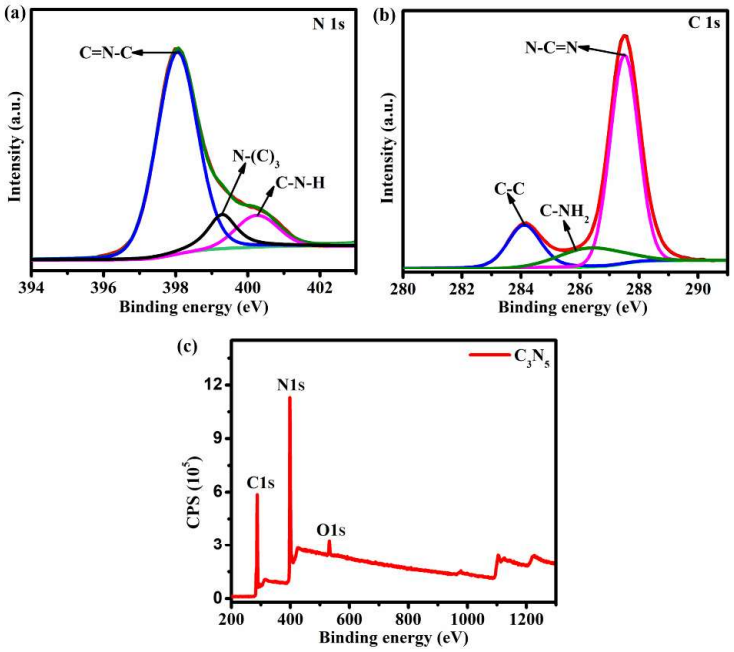

Figure 6. 3 *High-resolution deconvoluted elements* ***(a)*** *C1s,* ***(b)*** *N1s,* ***(c)*** *XPS survey of* C_3N_5

In ***Figure 6.3(a)*** and ***6.3(b)***, high-resolution elemental scans for N and C are depicted, that are further deconvoluted into individual valence states. In the C1s spectrum, the binding energy peaks at 284.6 eV, 286.1 eV, and 288.2 eV correspond to C-C, C-NH_2, and sp2 hybridized carbon within the aromatic ring (N-C=N), respectively. In the high-resolution

N1s spectrum, the binding energy peaks at 398.7 eV, 400.0 eV, and 400.8 eV are indicative of C-N=C, N-(C)3, and C-NH bonds, respectively[63]. It's worth noting that the presence of the peak at 400.8 eV in the N1s spectrum signifies the -NH group, underlining its role as an electron-donating group within the C_3N_5 structure.

6.3.1.5. Morphological Study:

Further, the morphological characteristics of the synthesized powder material as well as exfoliated C_3N_5 were comprehensively investigated using SEM, as presented in ***Figure 6.4(a)* & (b) respectively**. The SEM image in ***Figure 6.4(a)*** showcases a densely packed layered structure of bulk C_3N_5, aligning with the well-established feature as a two-dimensional (2D) layered material.

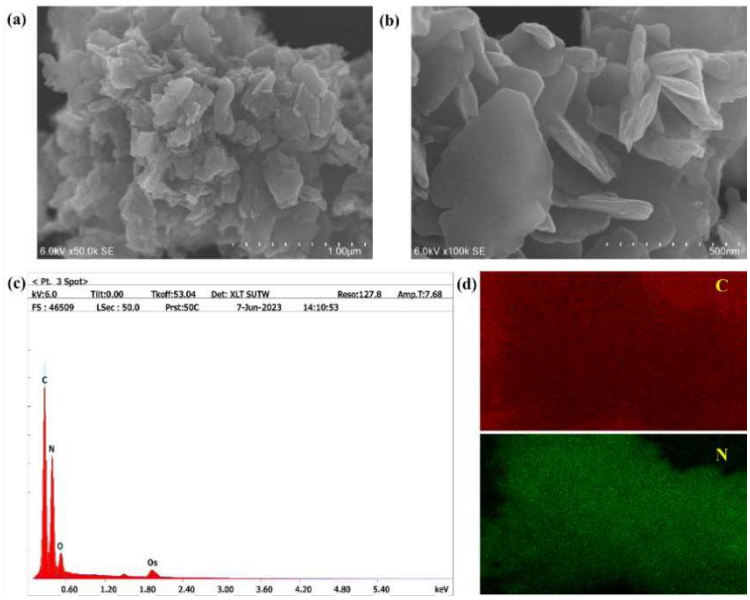

Figure 6. 4 *Represents the Sem image of* ***(a)*** *bulk* C_3N_5 ***(b)*** *exfoliated* C_3N_5 ***(c)*** *elemental survey of* C_3N_5 ***(d)*** *represents the elemental mapping of carbon and nitrogen.*

To confirm the elemental composition and their distribution, elemental mapping was conducted using the same instrument, as shown in ***Figure 6.4(d)*,** and the EDAX result has been provided in the ***Figure 6.4(c)*.** Upon subjecting the material to intense sonication, these densely packed layers underwent exfoliation, resulting in the formation of single or a

few layers of C_3N_5, as shown in ***Figure 6.4(b)***. Hence, it has been well evidenced by the successful synthesis of C_3N_5 and its exfoliation into nanosheet like morphology. These exfoliated C_3N_5 homogeneously dispersed into chloroform was then utilized to prepare the polymer hybrid blend with DPP-TTT and their thin films.

6.3.2. Characterization of DPP-TTT/C_3N_5 Blend Solution:

Figure 6.5, illustrates the FTIR spectrum of both the DPP-TTT and DPP-TTT/C_3N_5 hybrid solution, revealing a series of notable peaks and their corresponding vibrational modes. The distinctive peak at 3429 cm^{-1} signifies the stretching vibration of the −OH group, indicative of the presence of hydroxyl (-OH) functional groups that could be because of adsorbed moisture[192]. Notably, the emergence of the 801 cm^{-1} peak is attributed to the out-of-plane bending vibration of the C−H bonds, primarily originating from the thiophene rings within the polymer structure. The peak at 1107 cm^{-1} corresponds to the stretching vibrations of CN bonds, indicating the presence of cyno (-CN) groups in the material. Peaks at 1225 cm^{-1} (C−H stretching) and 3072 cm^{-1} (C−H bending) are linked to vibrations induced by the presence of chloroform molecules, offering information about the interaction between the material and the surrounding environment. The FTIR spectrum also reveals a peak at 2855 cm^{-1}, associated with the symmetrical stretching of saturated C−H bonds, and another peak at 2925 cm^{-1} attributed to the asymmetrical stretching of C-H bonds within the thiophene ring. These vibrations provide valuable insights into the molecular structure and bonding configuration of the polymer. In the DPP-TTT/C_3N_5 hybrid, additional peaks appear between 3380-3093 cm^{-1}, associated with the stretching vibration of surface-free amino groups. There is a shift in the (C-H) stretching visible, pristine DPP-TTT shows at 1225 cm^{-1} while DPP-TTT/C_3N_5 shows at 1241cm^{-1}. The emergence of an extra peak at 890 cm^{-1} in the hybrid material is indicative of the characteristic stretching vibration of the s-triazine ring unit, signifying the incorporation of C_3N_5. Additionally, a shift in the out-of-

plane bending vibration of the C−H bonds is observed, moving from 801 cm^{-1} in the pristine DPP-TTT to 807 cm^{-1} in the hybrid material. These changes in the DPP-TTT/C_3N_5 blend offer evidence of the interaction between C_3N_5 and the surrounding environment, contributing to a comprehensive understanding of the composite's surface chemistry.

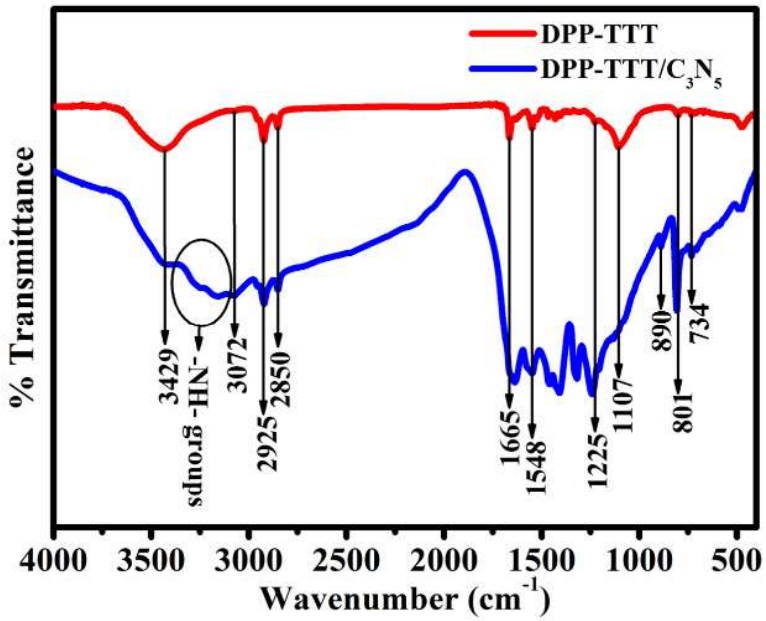

Figure 6. 5 *FTIR spectra of DPP-TTT/C_3N_5 blend solution.*

6.3.3. DPP-TTT/C_3N_5 Thin Film Characterizations:

6.3.3.1. XRD Analysis:

To investigate the impact of C_3N_5 on the crystallographic properties of DPP-TTT thin films, out-of-plane grazing incidence X-ray diffraction (GI-XD) patterns were obtained for the untreated thin films of pristine DPP-TTT and for the optimal DPP-TTT/C_3N_5(3%) mixture. As presented in ***Figure 6.6(a)***, a set of well-defined (*h*00) diffraction peaks are visible in both films, which indicates the presence of highly organized lamellar structures. Based on our prior observations and additional reports, semiconducting polymer thin films typically exhibit an “edge-on” type molecular arrangement when prepared using UFTM [91]. In the 'edge-on' arrangement, the polymer's alkyl side chains are observed to stack at a right angle

to the substrate surface, leading to the formation of multiple diffraction patterns along the q_z-axis. These observations provide confirmation of the substantial crystalline nature of the thin films, signifying a well-ordered and close packing of polymer chains. Nonetheless, some significant changes can be noticed in the (100) peak for these two thin films as shown in ***Figure 6.6(b)***. First, the intensified peak in the case of DPP-TTT/C_3N_5(3%) thin film corroborates the enhanced crystallinity and relatively more ordered structure compared to the pristine polymer films. Secondly, a higher angle shift ($\Delta\theta \sim 0.18°$) in the peak position indicates a reduction in interplanar spacing (d_{h00}). Thus, incorporation of exfoliated C_3N_5 as a filler within the DPP-TTT matrix notably resulted in enhanced structural coherence within the hybrid thin film, and hence C_3N_5 serve as templates for a superior self-assembly of DPP-TTT over the air-liquid interface. To quantitatively examine the impact of 2D nanosheets on the crystalline characteristics of thin films, we calculated the correlation length 'Lc' of reflection peaks to estimate the average crystallite size using the Scherrer equation. While Scherrer's equation is typically used to determine crystallite dimensions, the disordered nature of CP crystallites complicates precise measurements. Consequently, we refer to this measure as the coherence length Lc, which serves solely for comparing crystallite sizes between the samples. The coherence length of the hybrid film was approximately twice that of the pristine polymer films Achieving a higher coherence length in DPP-TTT/C_3N_5 thin films indicates greater crystallinity, which directly enhances charge transport efficiency. This increase in coherence length typically points to larger crystalline domains and fewer grain boundaries, enabling more efficient charge movement across the material[40]. Charges are better able to travel through these ordered regions because they encounter fewer defects and scattering points. Additionally, the larger coherence lengths contribute to improved stability and operational consistency in organic devices. With larger crystalline domains and enhanced molecular alignment, these materials exhibit fewer

structural irregularities. This reduction in defects leads to more consistent electrical properties and ultimately, boosts device reliability.

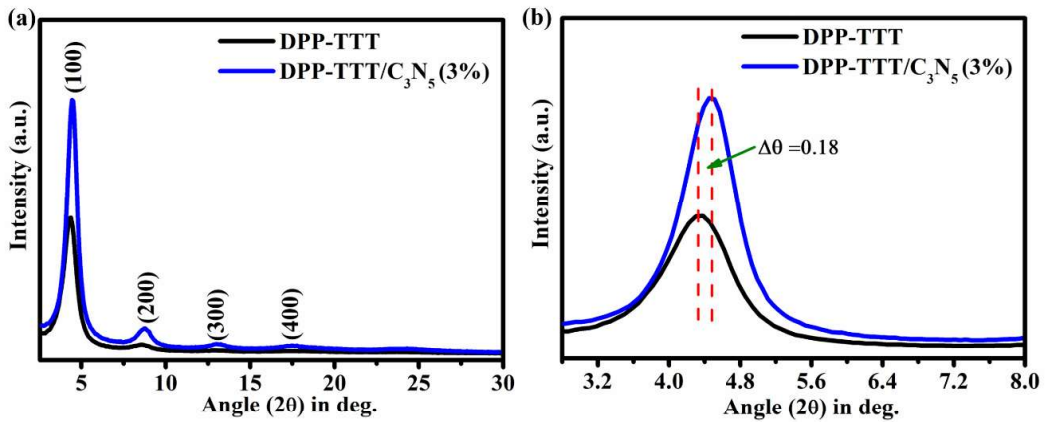

Figure 6. 6 (a) *GIXRD pattern of DPP-TTT and DPP-TTT/C_3N_5 (3%).* ***(b)*** *represents the shifting in the (100) peak of the DPP-TTT/C_3N_5 (3%) with respect to pristine DPP-TTT*

6.3.3.2. Optical Analysis:

Next, optical analysis was conducted to elucidate the influence of C_3N_5 on chain ordering, polymer chain aggregation, and the polymer's bandwidth in the hybrid material. To determine the molecular orientation of the film, measurements were taken in two orientations: parallel and perpendicular to the polarizer, as illustrated in ***Figure 6.7(a)***. The molecular orientation was ascertained by calculating the dichroic ratio (DR)of thin film as shown in ***Figure 6.7(b)***, defined as DR = (A∥)/(A⊥) a. Here, (A∥) represents the absorption with the polarizer aligned parallel (∥) to the polymer orientation, and (A⊥) indicates the absorption with the polarizer aligned perpendicular (⊥) to the polymer orientation. At a wavelength of 830 nm, the DR ratio was found to be 3.5. These DR ratios provide additional confirmation of the molecular orientation within the thin film, following the initial validation via UV-Visible spectroscopy. In the recorded spectra, two distinct peaks were observed at 830 nm and 753 nm, corresponding to A_{0-0} and A_{0-1}, respectively [193], as illustrated in ***Figure 6.7(c)***. With an increase in the fraction of C_3N_5 in the polymer, a slight

reduction in the shoulder peak at 753 nm was observed compared to the normalized 830 nm peak, indicating a more ordered π-stacking in the hybrid material. As per the Spano model[194], this types of molecular stacking often termed as the J-type aggregation, which is prominent in DPP-TTT because of π-π and donor-acceptor interaction causes densely packed rigid rod like structures. The modified Franck-Condon analysis was applied to extract meaningful insights into the packing order of aggregates in polymers. This was accomplished by analyzing the vibronic progression ratios between the A_{0-0} and A_{0-1} peaks in relation to the exciton bandwidth. Typically, a decrease in the A_{0-0} /A_{0-1} peak ratio, leading to a broader exciton bandwidth (W), signifies an increase in interchain Coulombic interactions and a reduction in intrachain excitonic interactions as previously reported by Venkatesh, Rahul, et al[194, 195]. The correlation between the vibronic progressions of the A_{0-0} and A_{0-1} peaks and the exciton bandwidth, as inferred from the modified Franck-Condon analysis, is depicted in ***Figure 6.7(d)***, offers insights into how the photophysical aggregates are organized based on variation of C_3N_5 concentration. The decrease in the A_{0-0} /A_{0-1} ratio and redshift associated with the increasing C_3N_5 fraction in the polymer provide evidence for the presence of J-aggregates. Interestingly it has been found that, up to 3% loading of C_3N_5 causes the highest ordering and smallest excitonic binding energy in the hybrid thin film, while the ordering decreases with further loading. It is needless to say that a J-type aggregation and their uniaxial orientation in hybrid material thin film leads to an enhanced charge transport in planar devices [93].

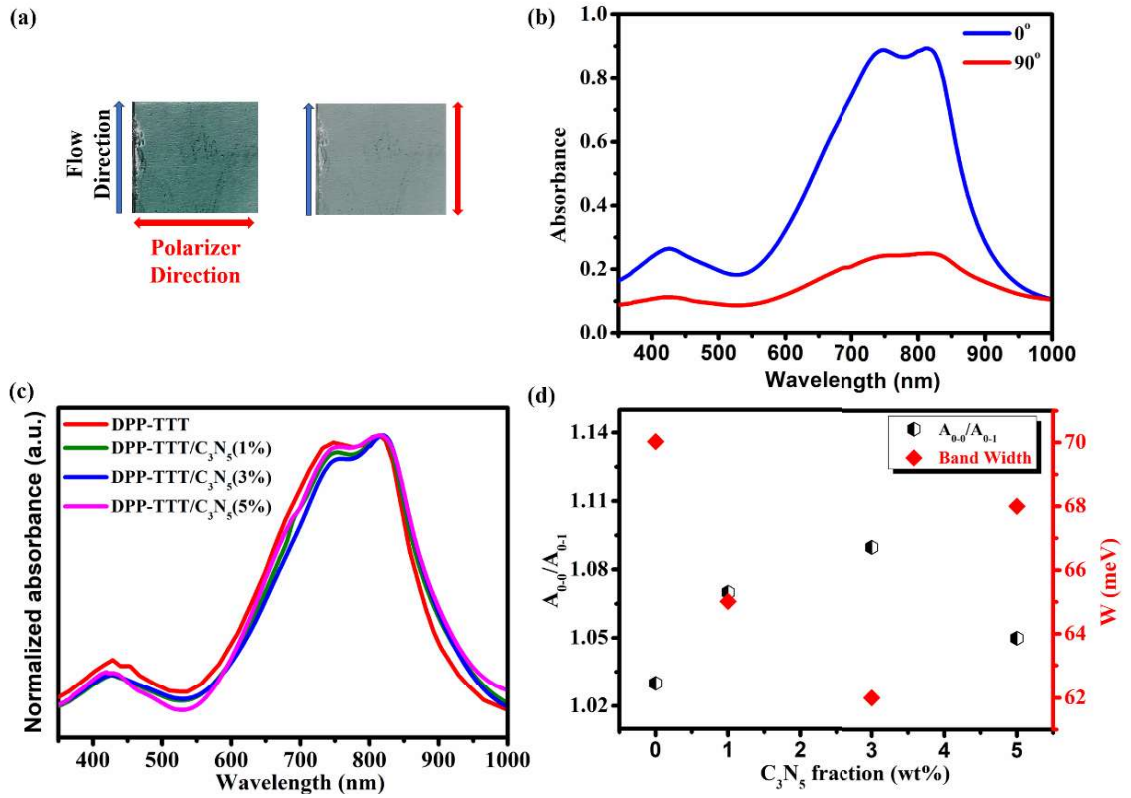

Figure 6. 7 ***(a)*** *represents the thin film with polarizer red double-sided arrow shows the direction of polarizer and blue arow presents the direction of flow.* ***(b)*** *Polarized spectra of thin film,* ***(c)*** *Normalized UV-VIS absorption spectrum of DPP-TTT and DPP-TTT/ C_3N_5 hybrid film.* ***(d)*** *$A_{0\text{-}0}/A_{0\text{-}1}$ ratio (black half-filled hexagonal) and exciton bandwidth (red diamond) as a function of C_3N_5 (wt.%) concentration in DPP-TTT.*

6.3.3.3 Morphological Characterization:

To assess surface morphology, and molecular orientation in those thin films, AFM height profiles were scanned in a 5×5 μm^2 area. ***Figures 6.8 (a) & 6.8 (b)*** presents the AFM height profile of DPP-TTT thin film, illustrating oriented domains. Shifting focus to ***Figures 6.8 (c) & (d),*** the AFM height profile image of the DPP-TTT/C_3N_5(3%) thin film shows densely packed domains oriented along a particular direction. Because DPP-TTT molecular assembly over air-liquid interface was supported by C_3N_5 nanosheets acting as physical template, and it influenced the overall film structure in hybrid thin film. Regarding surface roughness, the pristine polymer thin film displays an average roughness of 1.25 nm. In contrast, in the DPP-TTT/C_3N_5 hybrid thin film, the average roughness increases to 3.25

nm. This slight increase in roughness can be attributed to the incorporation of C_3N_5 nano sheets which increased the structural coherence and aggregation probability in hybrid thin films, as also evidenced from the XRD and UV-vis results.

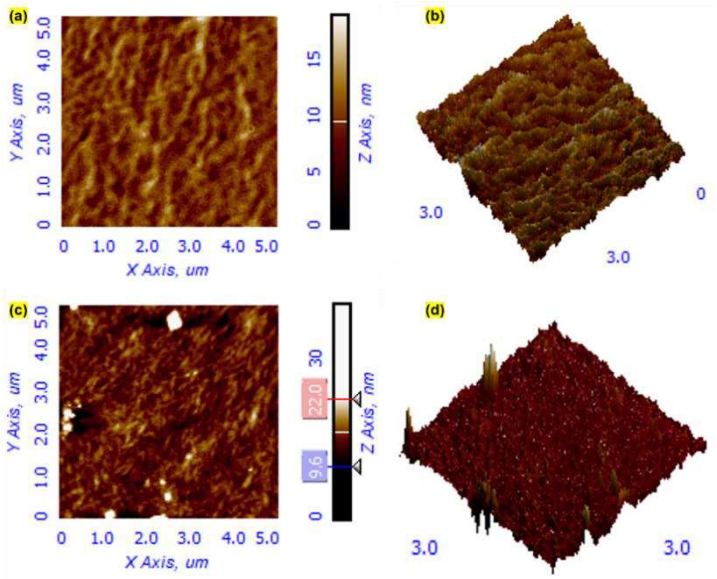

Figure 6. 8 ***(a) & (b)*** *AFM height profile and its 3D image of the DPP-TTT thin film, respectively,* ***(c) & (d)*** *AFM height profile and corresponding 3D image of the DPP-TTT/C_3N_5(3%) hybrid thin film, respectively.*

6.3.3.4. Cyclic Voltammetry:

To evaluate the impact of C_3N_5 on the electronic structure of the polymer thin film, we conducted a CV experiment, and the results have been displayed in ***Figure 6.9***. The results revealed distinctive features differentiating the pristine DPP-TTT from the hybrid thin films. Pristine DPP-TTT thin film exhibited a broad redox peak at approximately 0.97 V with onset potential (E_{ox}) at approximately ~0.83 V. Whereas the DPP-TTT/C_3N_5(3%) hybrid thin film displayed an oxidation peak at around 0.95 V with a slightly lower onset, E_{ox}~0.79 V, compared to the pristine one. The HOMO level of the samples was determined using the formula $E_{HOMO} = (E_{ox} + 4.4)\ eV$ [54]. Pristine polymer thin film displayed a HOMO level of approximately 5.23 eV, whereas the DPP-TTT/C_3N_5(3%) hybrid thin film exhibited a slightly lower HOMO level of about 5.19 eV. This decrease in

the HOMO level is likely attributable to the decrease in the ionization potential of hybrid thin films, resulting from an elevated degree of molecular ordering in contrast to pristine DPP-TTT films [196].

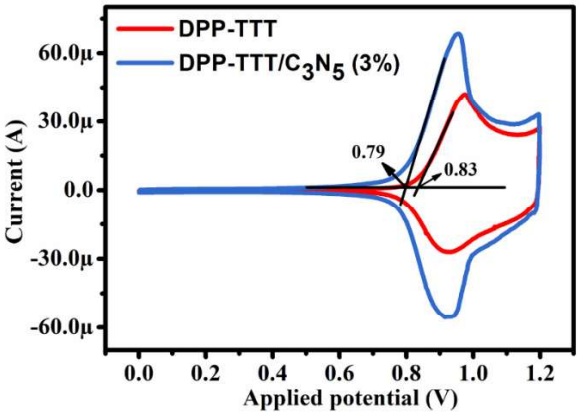

Figure 6. 9 *CV curve of DPP-TTT and DPP-TTT/C_3N_5(3%) hybrid thin film.*

6.3.4. Electrical Characterization of OFETs

I used the UFTM to fabricate OFETs to investigate the influence of C_3N_5 nanoflakes on the electrical characteristics of a thin film featuring aligned molecules. This setup ensured the polymer domain's orientation direction was parallel to the channel that forms between the source and drain electrodes, and schematics of OFETs are given in ***Figure 6.11(a).*** Electrical characterization of the OFETs was conducted at room temperature under 50% relative humidity conditions in a light-attenuated environment, employing a Keithley (2612) source meter. ***Figure 6.10(a)*** illustrates the output characteristics of the DPP-TTT polymer, while ***Figure 6.10(b)*** depicts the output characteristics of the OFETs based on the DPP-TTT/C_3N_5 (3%) nanohybrid thin film. The observed output characteristics confirm the P-channel behavior of the transistor.

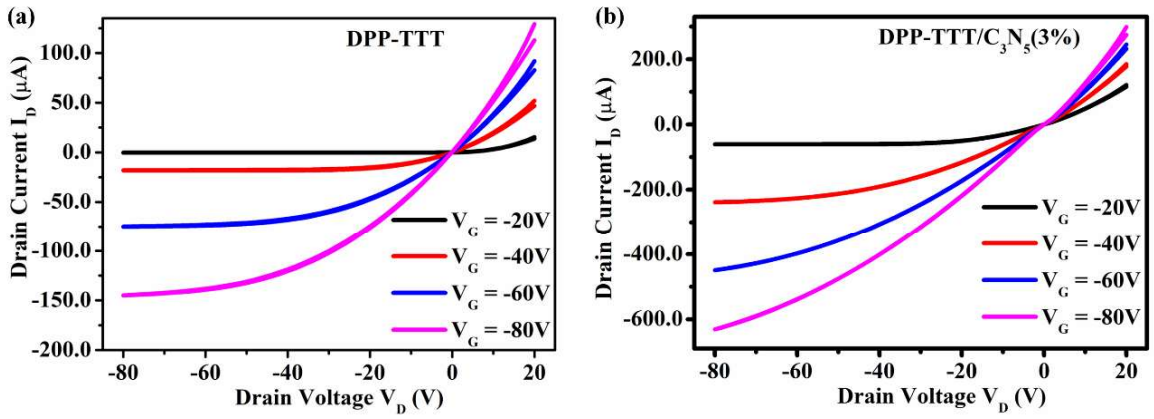

Figure 6. 10 ***(a)*** *Output characteristics of DPP-TTT* ***(b)*** *Output characteristics DPP-TTT/C_3N_5 (3%)*

Figure 6.11(b) presents the transfer characteristics of both the DPP-TTT polymer and the polymer nanohybrid thin OFETs with C_3N_5 nanoflakes incorporated into the polymer. Additionally, ***Figure 6.11(c)*** shows the $I_D^{1/2}$-V_G relationship of DPP-TTT/C_3N_5 OFETs. To determine the saturated field-effect mobility (μ_{sat}) and threshold voltage of the device, we employed a linear equation fitting approach to the $I_D^{1/2}$-V_G curve, as specified by the ***equation 6.1***[66].

$$I_{DS} = \frac{W\mu_{sat}C_{ox}}{2L}(V_G - V_{TH})^2 \qquad (6.1)$$

In the given equation, I_{DS} stands for the saturated drain current, C_{ox} is the areal capacitance of the dielectric, measured at 10 nf/cm^2. V_{TH} is the threshold voltage. (L) and (W) represent the channel length (30 μm) and width (2.8 mm), respectively. Additionally, μ_{sat} denotes the saturation field-effect mobility, and V_D and V_G are the potential differences between the drain and source, and the gate and source, respectively.The pristine DPP-TTT-based Field-Effect Transistor (FET) demonstrated an average saturation mobility (μ_{sat}) of approximately 0.11 cm²/V.s. However, upon introducing C_3N_5 nanosheets into the DPP-TTT polymer matrix, a notable modulation in the mobility of the resulting DPP-TTT/ C_3N_5 composite devices was observed as shown in ***Figure 6.11(d)***. For DPP-TTT/ C_3N_5 (3%)

composite devices a substantial enhancement of mobility to 0.49 cm²/V.s.

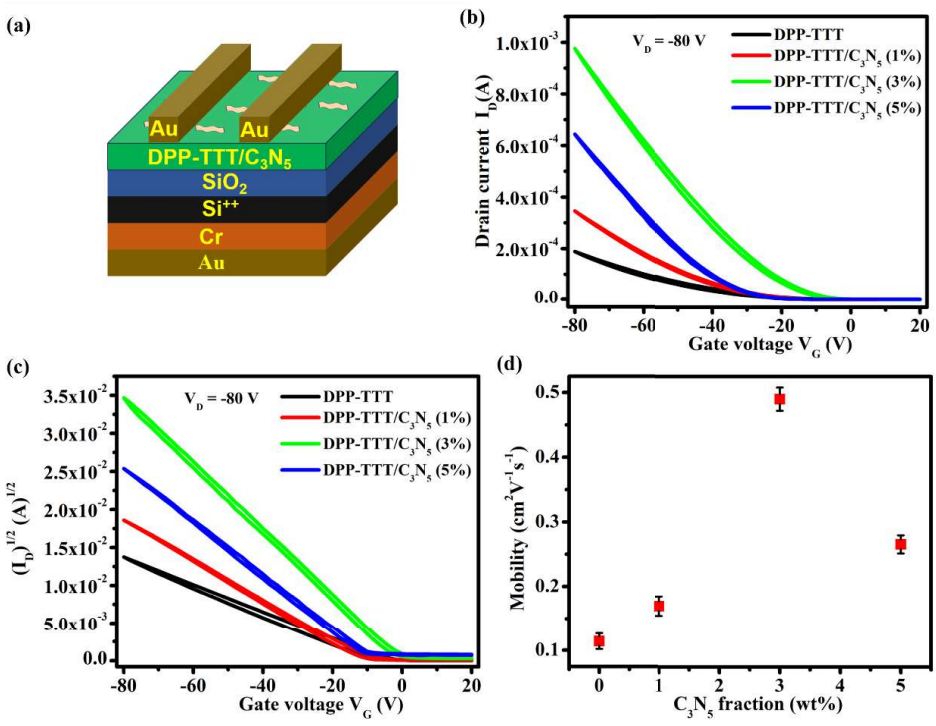

Figure 6. 11 ***(a)*** *Represents the device schematic* ***(b)*** *Transfer characteristics of DPP-TTT/C_3N_5* ***(c)*** *square root I_D-V_G of DPP-TTT/C_3N_5.* ***(d)*** *represents the mobility v/s C_3N_5 fraction.*

This enhancement can be attributed to several interrelated mechanisms. Firstly, the integration of C_3N5 sheets facilitates improved charge transport by creating efficient pathways, leveraging the high aspect ratio and conductive properties of C_3N_5 to reduce the energy barriers associated with charge carrier hopping between polymer chains. Concurrently, the morphological optimization achieved by the inclusion of C_3N_5 promotes a more ordered arrangement of the polymer chains, enhancing π-π stacking interactions critical for charge transport [52]. Moreover, the interface between C_3N_5 sheets and the DPP-TTT matrix plays a pivotal role in modifying the local electronic structure, thereby potentially lowering energy barriers for charge injection and enhancing overall mobility. Additionally, this composite material exhibits a decreased density of trap states, further facilitating seamless charge carrier flow by minimizing capture and immobilization. To

gain a comprehensive understanding of the observed mobility enhancement, a thorough evaluation of structural qualities, alignment, and orientation influencing mobility is necessary. The relatively small on/off ratio in the DPP-TTT/ C_3N_5 scenario can be rationalized by considering measurement conditions and the concentration of 2D nanosheets. The presence of acceptor moieties in the DPP-TTT polymer restricts the on-off ratio to 10^5, and 2D nanosheets further exacerbate the decline in the on-off ratio[197].

6.3.5 SHG Measurement

Electric field-induced second harmonic generation (EFISHG) measurements offer a direct method to visualize the motion of injected carriers. When a step voltage pulse with a duration of 100 nanoseconds is applied, carriers are injected from the source electrode into the organic semiconductor layer. Subsequently, these carriers undergo transportation between the two electrodes. The existence of these carriers induces the generation of an electric field within the organic semiconductor. As a result, SHG light is emitted, a phenomenon that can be attributed to the third-order nonlinear optical susceptibility of the organic compounds. [70]. To measure SHG, a positive voltage pulse of 120 V was applied to the source electrode. Meanwhile, both the gate and drain electrodes were short-circuited and connected to the ground, as depicted in ***Figure 6*.12**, a significant observation was made at the onset of the experiment.

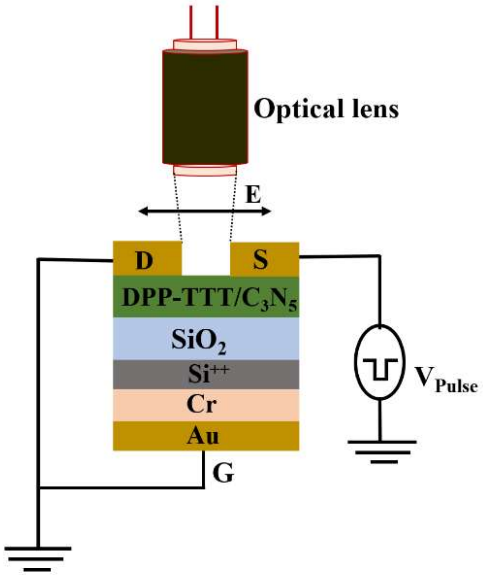

Figure 6. 12 *Optical configuration for Second Harmonic Generation (SHG) analysis, and the sample architecture for Field-Effect Transistor (FET) evaluations.*

At an exact delay time of 0 nanoseconds, the laser pulse was synchronized with the initial rise of the voltage pulse, as observed in ***Figure 6.13***. At this juncture, Second Harmonic Generation (SHG) signals emerged near the source electrode's boundary, signifying the commencement of carrier injection. Sequential imaging strikingly showed that the emission band of the SHG signal progressively shifted across the channel, moving from the source towards the drain electrode as the delay time increased. The observed progression of the emission band from the source electrode, rather than the drain, offers conclusive proof of hole injection from the gold source electrode. This is indicative of a low barrier to injection. This phenomenon indicates that the DPP-TTT/C_3N_5-based OFETs exhibits p-type conductivity and enters an 'on' state upon the application of a positive voltage. This capability stands out as a significant advantage, offering a direct observation method that the TRM-SHG technique facilitates, allowing for the precise determination of carrier types in the OFETs device.

The luminous cloud's position and brightness reveal the location and density of holes at any given moment. ***Figure 6.13 (a) & 6.13 (b)*** display the precise positions of carriers (holes)

at a specific time following the application of a -120 V pulse for DPP-TTT and DPP-C_3N_5 (3%), respectively. A prominent bright horizontal line near the bottom marks the location of the source electrode. As time progresses, this luminous cloud ascends towards the drain electrode. The darker patches or regions observed in these images can be attributed to the morphology of the deposited films. The absence of light in these areas is due to the fact that the emitted light was not at an oblique angle, and therefore, was not captured by the detector. The Figures clearly demonstrate that the injection of carriers occurs smoothly across all the films. A detailed examination of these images reveals that the carriers move quickly at first. Yet, as they move further away from the electrodes, their pace noticeably slows down. This phenomenon can be ascribed to a reduction in Coulombic repulsion, stemming from changes in carrier concentration over time. In the case of Pristine DPP-TTT as shown in ***Figure 6.13 (a)***, both the carrier movement and carrier density appear to be slower when compared to the DPP-TTT/C_3N_5 blend as shown in ***Figure 6.13 (b)***. Within 100 nanoseconds, carriers are seen reaching the drain electrode in the DPP-TTT sample. In both cases, the cloud becomes more evenly dispersed near the end as the carrier movement gets progressively less acute. This means that the carriers are distributed uniformly. The DPP-TTT/C_3N_5 blend shows a significant improvement in mobility compared to pure DPP-TTT. The mobility value rises from 0.06 to 0.31 $cm^2/V.s$ (measured 100 nanoseconds after the carriers are injected). The mobility was calculated by using ***equation 6.2*** [86]

$$\boldsymbol{x = \sqrt{2 \times V \times \mu \cdot t}} \qquad \textbf{(6.2)}$$

Where x is the peak position, V is applied voltage, μ is mobility and t are time interval. This method allows us to accurately track the carrier locations in both space and time dimensions, and measure how fast they move under an electric field. To compare the values in a fair way, we choose a reasonable time interval of 100 nanoseconds. The mobility value drops sharply because the carriers need to hop between different crystal regions to cover

the whole length. Charge entrapment also results from structural instability, flaws, and inadequate interconnectivity, which reduces the mobility of conducting polymers during motion. I calculated average mobility values by analyzing the OFETs transfer characteristics in order to explore the charge transport dynamics in more detail.

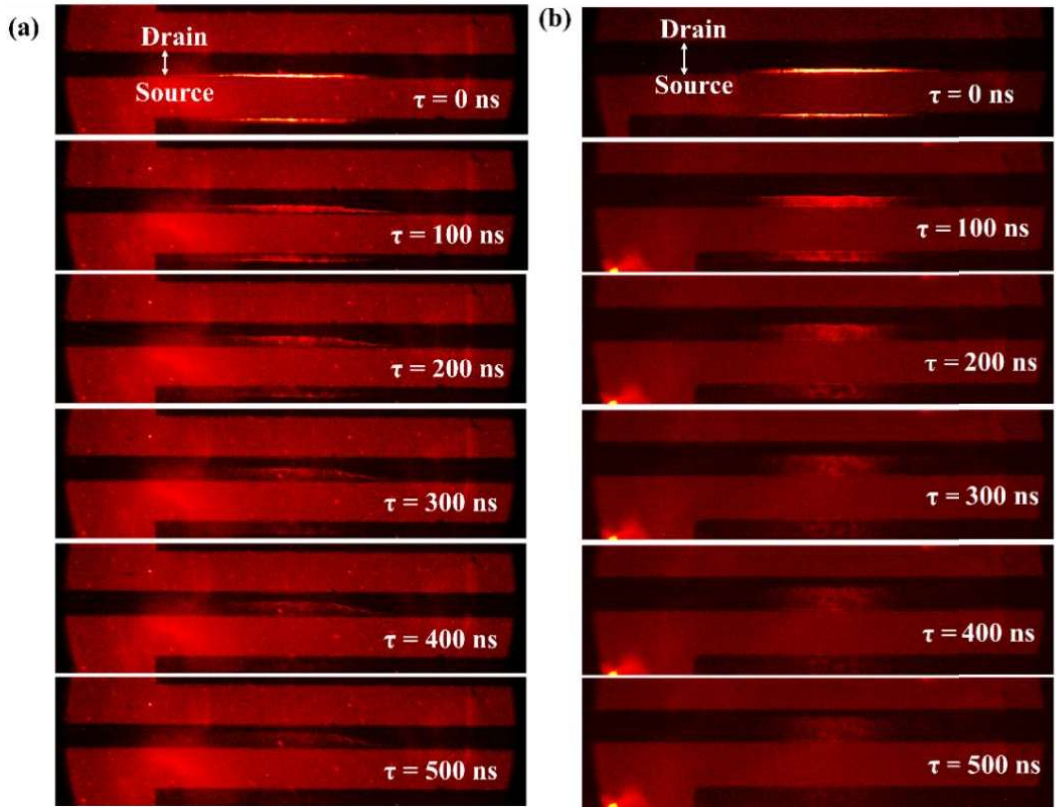

Figure 6. 13 *SHG image of* ***(a)*** *DPP-TTT OFETs with different time interval* ***(b)*** *SHG image of DPP-TTT/C_3N_5 OFETs with different time interval.*

In the investigation of the charge transport behavior in polymer-based composites, the integration of two-dimensional (2D) materials emerges as a pivotal strategy to enhance electrical properties and device performance. The comparative analyses of the DPP-TTT polymer and its composite with C_3N_5 2D sheets, as depicted in ***Figure 6.13***, offer profound insights into the mechanistic enhancements provided by 2D materials in polymer matrices. The time-resolved images further corroborate these findings, where the visual data from the DPP-TTT/C_3N_5 composite under various time frames show a more homogeneous intensity across the device. This uniformity in SHG signal is indicative of a smoother, more

uniform charge flow, underscoring the effectiveness of the 2D sheets in modulating the electronic properties of the polymer.

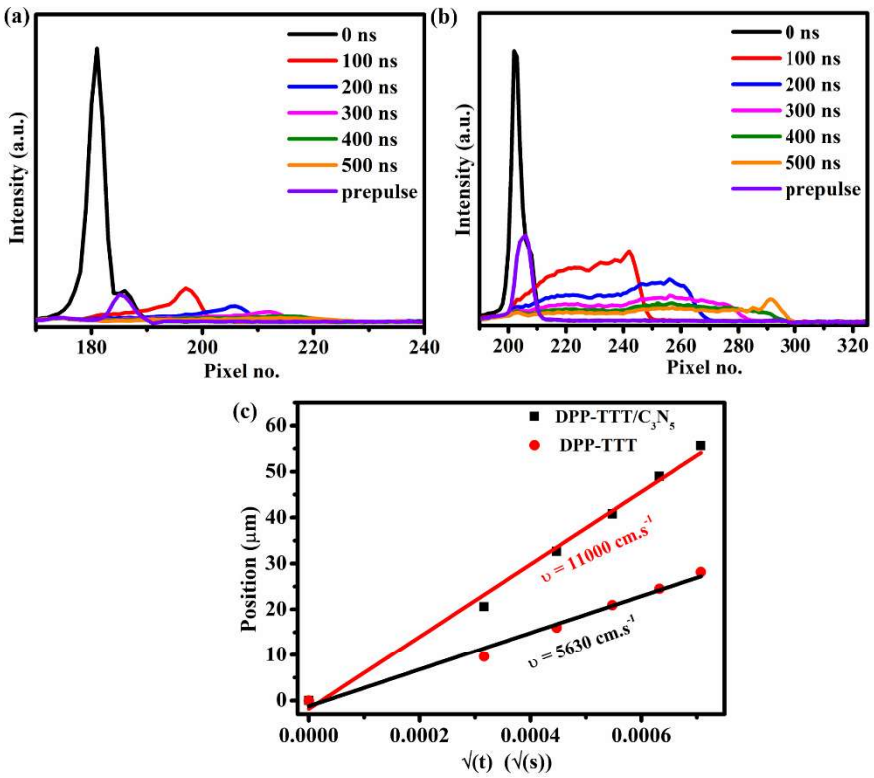

Figure 6. 14 (a) *Represents the pixel position of DPP-TTT OFET under different time interval,* ***(b)*** *Represents the pixel position of DPP-TTT/ C_3N_5 (3 %) OFET under different time interval,* ***(c)*** *Presents the position of the charge carrier of DPP-TTT and DPP-TTT/C_3N_5 calculated from the SHG image*

Further these carrier distributions were plotted with pixel number as shown in ***Figure 6.14 (a & b)***. The image illustrates significant distinctions in charge carrier distribution between the pure polymer and the composite material. In the pure polymer DPP-TTT, charge distribution exhibits a high degree of localization, as evidenced by the sharp, irregular peaks in intensity across the pixel range over time as shown in ***Figure 6.14(a)***. This behavior indicates the presence of substantial trap states within the polymer matrix, which localize charge carriers, impeding their uniform distribution and free movement. These trap states, often associated with structural imperfections or molecular disorientation, severely restrict the efficiency of charge transport across the polymer matrix. Conversely, the DPP-

TTT/C_3N_5 device demonstrates a markedly improved charge distribution. The intensity profiles from the composite samples display a more flattened and uniform distribution over time, suggesting a dynamic and efficient charge transport pathway. The role of C_3N_5 sheets can be attributed to their ability to fill the inherent trap states in the polymer matrix. The molecular structure of the 2D sheets likely provides alternate pathways for charge carriers, facilitating their movement by bypassing or neutralizing the trap states. Moreover, the 2D sheets enhance the overall structural alignment within the composite as confirmed by XRD and UV, promoting a more ordered arrangement of polymer chains which is conducive to charge mobility.

The integration of C_3N_5 2D sheets within the DPP-TTT polymer matrix is thus shown to be a critical factor in mitigating the limitations posed by trap states. By providing a more homogeneous charge distribution and filling trap states, the 2D sheets not only enhance the intrinsic electrical conductivity but also improve the operational stability and efficiency of the polymer-based devices. The enhanced mobility observed in composite films incorporating DPP-TTT and C_3N_5 can be attributed to several potential mechanisms, each contributing to the overall improvement in performance. These mechanisms include: (a) C_3N_5, with its unique structure, may directly enhance the composite's conductivity by introducing additional charge carriers or facilitating their movement. (b) The presence of C_3N_5 within the organic semiconductor matrix might facilitate charge transfer interactions, effectively improving the mobility of charge carriers by creating pathways for easier movement. (c) The C_3N_5 nanosheets could act as a conducting scaffold within the composite, particularly enhancing conduction in the polymer's amorphous regions, thereby improving overall mobility. (d) The integration of C_3N_5 may positively affect the interior morphology of the films, leading to a more favorable environment for charge carrier mobility. DPP-TTT inherently has a backbone prone to instability due to its alternating

single and double bonds. The introduction of C_3N_5 not only provides additional mobile carriers through a doping effect but also facilitates the delocalization of π-bonding electrons along the polymer's conjugated backbone, creating more efficient pathways for carrier movement. We also calculated the average carrier velocity[198] of DPP-TTT and DPP-TTT/ C_3N_5 (3%) transistors. The average charge carrier velocity for the DPP-TTT transistor was calculated 5630 cm/sec, while for DPP-TTT/C_3N_5 transistor was 11000 cm/sec from its pixel positions as shown in ***Figure 6.14 (a) & 6.14 (b)***, respectively, this charge carrier velocity also reveals the C_3N_5 works as conducting template to easy access the flow of charge carrier. All the values were calculated from the pixel position of SHG image with o nanoseconds to 100 nanoseconds. Pixel position with different time interval is given in the ***Figure 6.14 (c)***, for DPP-TTT and DPP-TTT/C_3N_5 (3%) transistor. However, the inherently narrow electronic energy bands in DPP-TTT pose a significant barrier to carrier motion, leading to slow electron movement, lattice distortion, and polarization, which in turn forms polarons with extended lifetimes. C_3N_5 acts as a semiconductor with zero band overlap, characterized by its capacity to host both holes and electrons as charge carriers. Its two-dimensional sp2 hybridized bonding leaves one electron unbound, available for conduction in the third dimension. This arrangement allows for the formation of protruding p-electron clouds, enhancing mobility through the graphene-like sheets. When C_3N_5 sheets are combined with DPP-TTT, their compatible surface energies encourage a lamellar packing structure, promoting π-π interactions between the chains[199]. This interaction distorts the crystal potential, creating localized levels near the LUMO and HOMO regions, which in turn facilitates additional polaron formation. Such π-π interactions increase the number of polarons within the lattice, altering the material's electrical properties in favour of enhanced mobility[200]. Although the smaller size of C_3N_5 sheets relative to the polymer chains suggests that the direct addition of electrons along the entire pathway might be

limited, the observed improvements in mobility suggest that C_3N_5's role is more significant in facilitating charge carrier movement rather than merely donating electrons. Previous studies have shown that the incorporation of functionalized fillers can improve mobility, but excessive additions often distort the structural integrity. In our research, the strategic addition of C_3N_5 at precise concentrations has successfully enhanced mobility without compromising the composite's structure, indicating a nuanced interplay of the aforementioned mechanisms in achieving the observed mobility enhancements.

6.4. Conclusion:

In conclusion, this chapter is dedicated to the development and analysis of OFETs based on a composite material combining DPP-TTT with C_3N_5, where C_3N_5 functions as conducting nanoflakes within the structure. The introduction of C_3N_5 into the DPP-TTT matrix was found to significantly enhance the carrier mobility compared to that of pure DPP-TTT. This improvement in mobility was analyzed through the application of EFI-SHG measurements. These measurements provided us with a direct method to visualize and quantify the enhancements in carrier mobility within the composite. The notable increase in carrier mobility is largely attributed to the role of C_3N_5 in promoting a more ordered lamellar packing structure within the composite. This ordered structure is believed to facilitate more efficient carrier transport across the OFETs. Our findings shed light on the critical impact of composite material design on the performance of organic electronic devices, especially OFETs. By offering deeper insights into how the integration of conducting nanoflakes like C_3N_5 can improve device performance through structural optimization, our research contributes to the broader field of material science and electronics, paving the way for the development of more efficient and high-performing organic electronic devices